Early Visual Experience Shapes Binocularity in the Mouse Thalamocortical Pathway

Carey Y. L. Huh[1], Karim Abdelaal[2], Kirstie J. Salinas[1], Diyue Gu[3], Jack Zeitoun[1], Dario X. Figueroa Velez[1], John P. Peach[4], Charless C. Fowlkes[5], Sunil P. Gandhi[1,6]*

AFFILIATIONS

[1]Department of Neurobiology and Behavior, University of California, Irvine, California 92697

[2]School of Biological Sciences, University of California, Irvine, California 92697

[3]Donald Bren School of Information & Computer Sciences, University of California, Irvine, California 92697

[4]Whiting School of Engineering, Johns Hopkins University, Baltimore, Maryland 21218

[5]Department of Computer Science, University of California, Irvine, California 92697

[6]Center for Neurobiology of Learning and Memory, University of California, Irvine, California 92697

*Corresponding author

CORRESPONDENCE

Sunil P. Gandhi

Department of Neurobiology and Behavior

University of California, Irvine

2146 McGaugh Hall

Irvine, CA 92697

Phone: (959) 824-9051

Email: sunil.gandhi@uci.edu

SUMMARY

Developing neural circuits are particularly vulnerable to alterations in early sensory experience. For example, monocular deprivation (MD) during a juvenile critical period leads to long-lasting changes in ocular dominance and spatial acuity in primary visual cortex. The locus of these changes has been widely considered to be cortical. However, recent evidence indicates that binocular integration may occur first in the dorsolateral geniculate nucleus of the thalamus (dLGN), leaving open the question of whether changes in early visual experience can affect binocularity in dLGN. Using *in vivo* two-photon Ca^{2+} imaging of dLGN afferents in superficial layers of mouse visual cortex, we demonstrate that critical-period MD selectively impairs binocularity in dLGN inputs while visual acuity in this pathway remains relatively intact. Our data suggest that alterations in cortical ocular dominance following critical-period MD may partially reflect binocularity loss in dLGN neurons, whereas acuity deficits first manifest in primary visual cortex.

Long-term monocular deprivation during the critical period of visual system development (MD) chronically alters ocular dominance[1–4] and impairs spatial acuity in the visual cortex[5,6]. Abnormal binocular vision and reduced acuity are the hallmarks of amblyopia, a visual disorder that arises from unbalanced binocular input during early childhood[7]. Early work using the MD manipulation demonstrated profound functional changes in primary visual cortex (V1), but findings in dLGN have been mixed with some reporting no functional changes[8–10] while others have shown cell-type specific deficits[11,12]. Anatomical changes in thalamocortical projections have been observed in MD models[13,14] and recent brain imaging studies indicate that human amblyopes display thalamic deficits[15,16]. Given these lines of evidence, functional and anatomical changes following critical-period MD in the thalamocortical circuit need to be re-examined.

Furthermore, emerging evidence indicates that significant binocular processing occurs in dLGN in mice[17–19] and marmosets[20]. A recent retrograde tracing study[21] demonstrated that single dLGN neurons receive direct retinal inputs from both eyes, providing an anatomical substrate for binocular integration in the mouse dLGN. A recent functional study[19] showed that ocular dominance of thalamic axons in V1 can be temporarily altered by short-term MD under plasticity-enhancing conditions in adult mice. However, it remains unknown whether MD during the critical period of development leads to long-lasting changes in ocular dominance and visual acuity of dLGN neurons.

To address this question, we performed *in vivo* two-photon Ca^{2+} imaging of thalamocortical axons from dLGN neurons sending projections to binocular V1 (bV1), in adult mice that were either monocularly deprived for 14 days during the critical period (P19-33) or littermate controls (Fig. 1b). The calcium sensor, GCaMP6s, was specifically targeted to thalamic neurons by injecting a Cre-dependent GCaMP6s virus into dLGN in VGLUT2-Cre mice (Fig. 1a; see Methods). Calcium imaging was performed in awake mice that were viewing drifting gratings of various orientations and spatial frequencies (Fig. 1c). Two-photon Ca^{2+} imaging was performed in superficial layers (L1-2/3) of bV1 (Fig. 1d-g). Mice were used for functional imaging in adulthood (P93 – 132, mean: P106) to characterize long-lasting alterations following critical-period MD. In MD mice, virus injection and imaging were performed on the hemisphere contralateral to the deprived eye.

Fig. 1. Selective loss of binocular thalamocortical boutons following critical-period MD

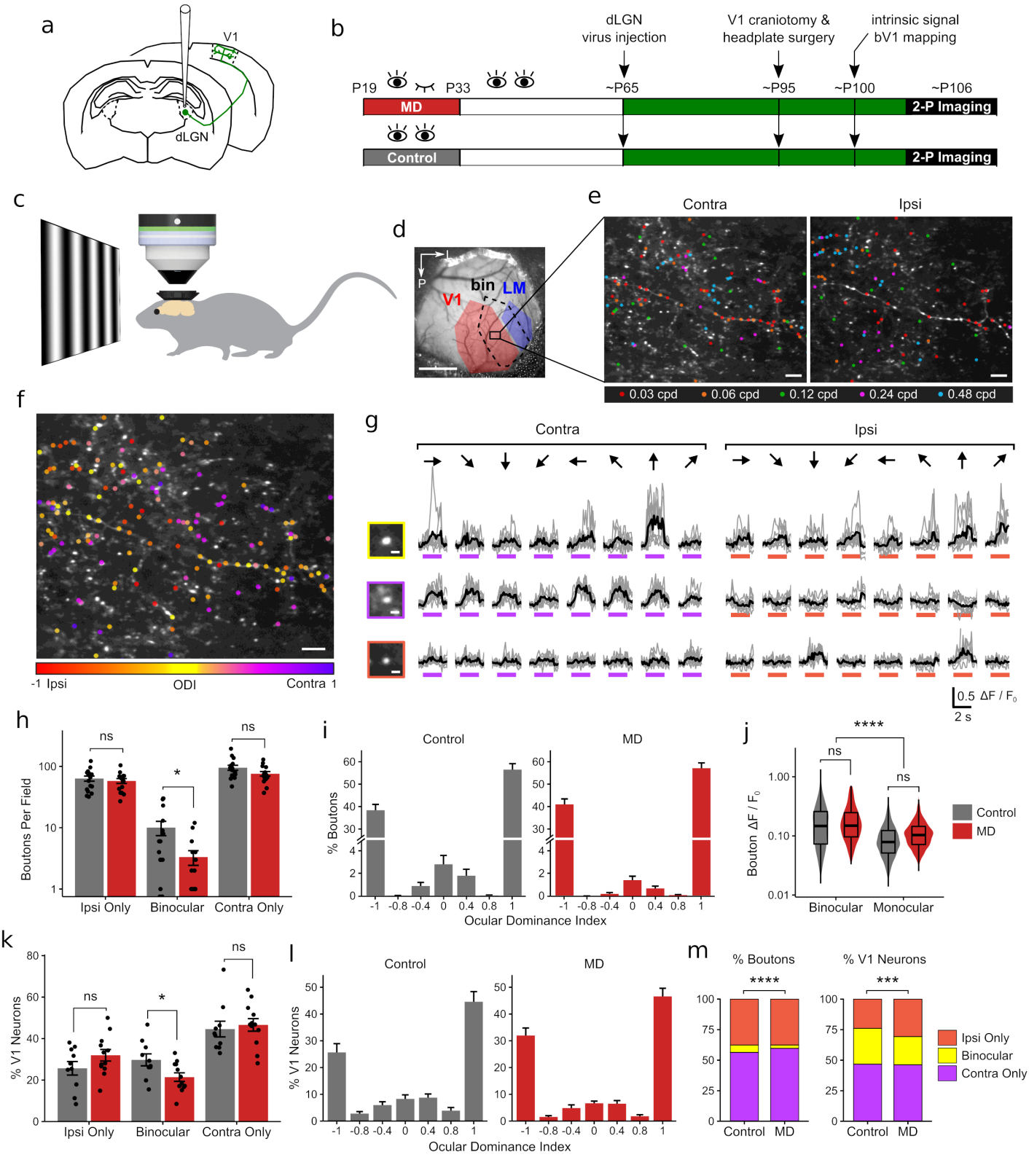

We found that most dLGN boutons in superficial layers of bV1 were monocular (visually responsive to contralateral or ipsilateral eye only) with a small fraction of boutons displaying significant visual responses to both eyes (binocular; 6% in control mice; Fig. 1e-g and Supplementary Fig. 3). To our surprise, we found that critical-period MD led to a selective reduction in the number of binocular dLGN boutons recorded per field of view (70% reduction; Fig. 1h-i). This was not due to reduced detectability of binocular boutons in MD mice, because there was no significant difference in response strength between control and MD mice (Fig. 1j and Supplementary Fig. 1). Interestingly, binocular boutons displayed on average twice stronger response amplitudes compared to monocular boutons (Fig. 1j, median R_{pref} for binocular boutons: 0.15, monocular boutons: 0.08). MD significantly reduced the binocular fraction among dLGN boutons from 6% to 3% in control *vs.* MD mice (Fig. 1m, left, and Supplementary Fig. 1). The number of virally infected neurons and their spatial distribution in dLGN were comparable between control and MD mice and could not explain the reduction in binocular boutons (Supplementary Fig. 2).

For comparison, we also examined the effects of MD on L2/3 excitatory neurons in bV1 by performing two-photon Ca^{2+} imaging from GCaMP6s-expressing cells in CaMK2a-tTA;tetO-GCaMP6s transgenic mice[22,23]. We found that critical-period MD led to a significant reduction in the percentage of binocular bV1 neurons from 29% to 23% in control *vs.* MD mice (Fig. 1k-m) without a significant reduction in response amplitude (Supplementary Fig. 1). These results suggest that MD-induced binocularity deficits observed at the level of V1 may originate, at least in part, from binocular dLGN input loss.

Following critical-period MD, mice develop reduced visual acuity in the deprived eye, an impairment that lasts well into adulthood[24–26]. It remains unclear whether acuity deficits are generated *de novo* in cortical circuits or are inherited from dLGN. It is also unknown how spatial frequency (SF) representation interacts with ocular dominance in dLGN. Previously, we showed that contralateral-eye dominated monocular V1 neurons prefer higher SF compared to binocular neurons[23]. Thus, we explored how binocularity and SF processing interact in dLGN boutons and whether critical-period MD affects these properties.

We found that dLGN boutons were tuned to a wide range of SF, varying from 0.03 to 0.96 cpd (Fig. 2 and Supplementary Fig. 3-4). As a population, dLGN responses were tuned to higher SF compared to V1 neurons (Fig. 2b-e and Supplementary Fig. 4), consistent with a

Fig. 2. Intact SF processing in thalamocortical boutons following critical-period MD

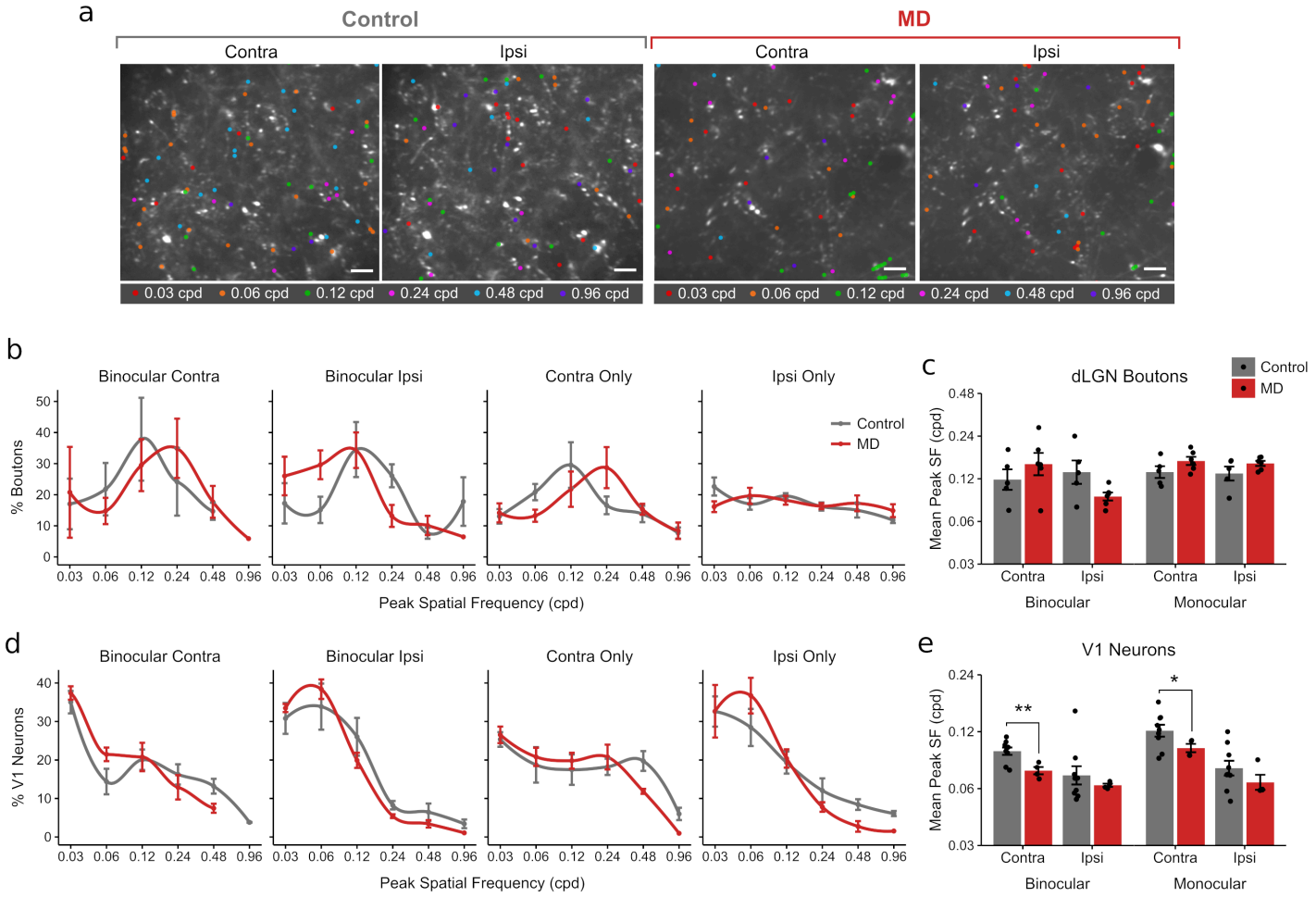

previous report[27]. Binocular boutons were tuned to significantly lower SF compared to contralateral-eye dominated monocular boutons, similar to our observations in V1 neurons[23] (Supplementary Fig. 4).

Interestingly, we found no statistically significant effect of critical-period MD on dLGN boutons' preferred SF (Fig. 2a-c). Boutons' SF tuning widths were comparable between control and MD mice and similar to those found in V1 neurons (Supplementary Fig. 5). In contrast, MD led to a robust reduction in preferred SF of V1 neurons, particularly for contralateral (deprived) eye responses (Fig. 2d-e). Significantly fewer V1 neurons preferred 0.48 – 0.96 cpd in MD mice compared to controls (Fig. 2d and Supplementary Fig. 5). These results indicate that critical-period MD significantly impairs visual acuity in V1 neurons while

Fig. 3. Interocular mismatch in thalamocortical boutons following critical-period MD

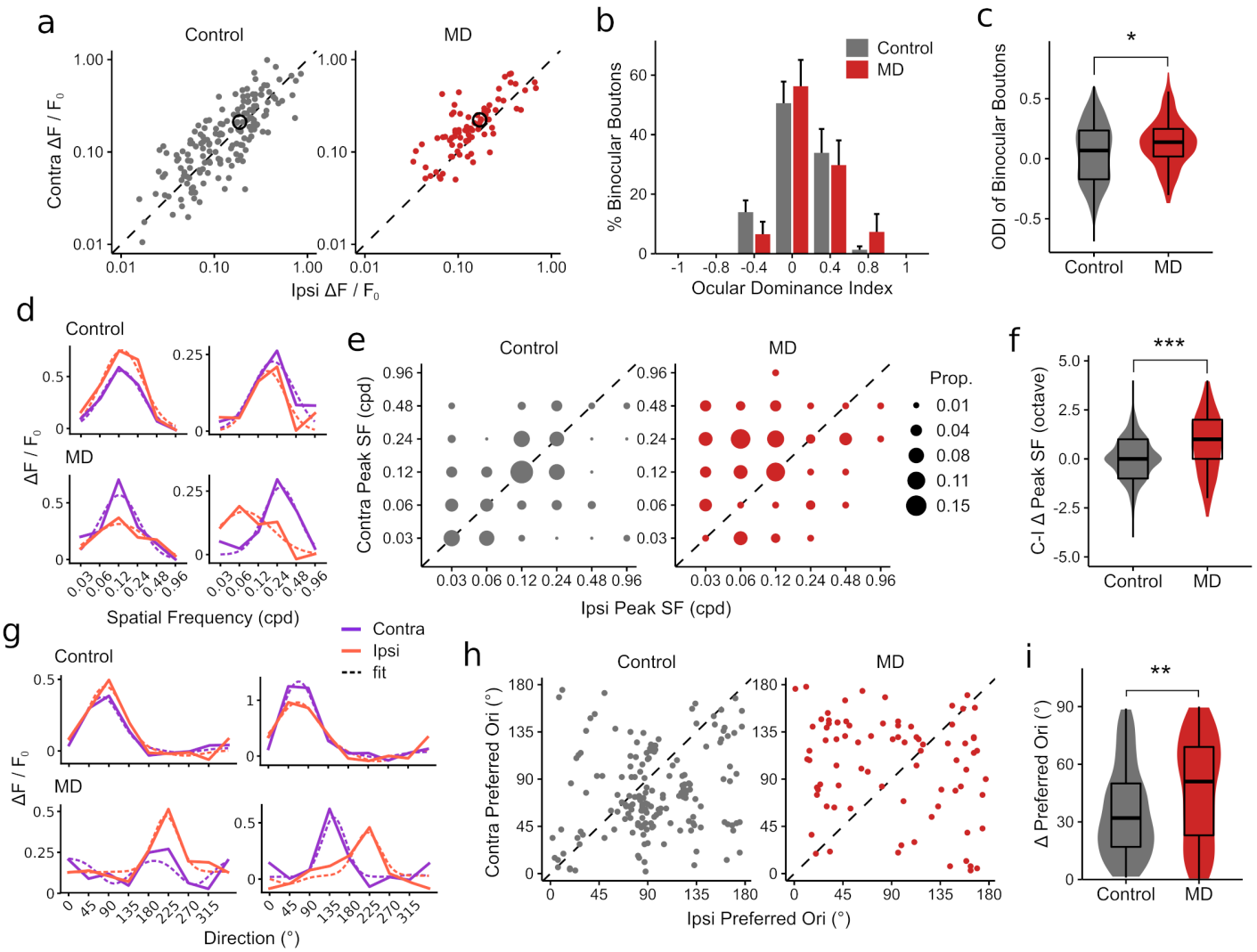

leaving SF processing in dLGN responses relatively intact. It suggests that binocular vision during the critical period is necessary for the development of visual acuity in V1 but not in dLGN.

Critical-period MD has been shown to lead to binocular mismatch of preferred orientation in V1 neurons[28–30]. Since we found a selective binocularity loss in dLGN boutons following MD (Fig. 1), we examined visual properties in the remaining binocular dLGN boutons in MD mice to assess additional functional deficits and interocular matching.

In controls, binocular dLGN boutons were well matched in terms of response amplitude and spatial frequency tuning (Fig. 3a-f and Supplementary Fig. 3). The majority (54%) of

binocular boutons displayed ocular dominance index (ODI) values between -0.2 and 0.2 (Fig. 3b), and 40% of binocular boutons showed exact peak SF matching between the eyes (Fig. 3d-f). Among SF-mismatched boutons, preferred SF was higher in contralateral- or ipsilateral-eye responses in approximately equal proportions of boutons (Fig. 3e and Supplementary Fig. 5). Binocular boutons also showed significant matching in terms of preferred grating orientation (Fig. 3g-i and Supplementary Fig. 3).

We found that critical-period MD led to greater inter-ocular mismatch in visual properties. Binocular boutons were less well matched in response amplitude between the eyes in MD mice and this was reflected in a small but significant change in ODI of binocular boutons towards the contralateral (deprived) eye (ODI shift: +0.09; Fig. 3b-c). We also found an increased magnitude of mismatch in preferred SF in MD mice, with ipsilateral (non-deprived) eye responses being tuned to lower SF compared to contralateral-eye responses in MD mice (Fig. 3d-f and Supplementary Fig. 5). The SF mismatch was not due to boutons exhibiting broader SF tuning in MD mice (Supplementary Fig. 5). MD also led to a higher degree of interocular mismatch in preferred orientation in binocular dLGN boutons (Fig. 3g-i). Overall, many dLGN boutons were highly direction-tuned (Supplementary Fig. 3, 4 and 6), consistent with known properties of dLGN neurons projecting to superficial layers of V1[31–33], and orientation/direction selectivity indices were similar between control and MD mice (Supplementary Fig. 6). These findings indicate that normal binocular vision during the critical period of development is necessary for proper interocular matching of visual properties in binocular dLGN neurons.

Considering that binocular dLGN inputs are selectively impaired following MD and they constitute a relatively small proportion of the total thalamocortical input (Fig. 1), we hypothesized that there would be little to no gross structural deficit in thalamocortical projections following critical-period MD. Indeed, we found no significant long-lasting alterations in the overall density and thickness of dLGN axons in V1 L1-2/3 in MD mice compared to controls (Supplementary Fig. 7), consistent with previous studies that used 7- or 20-day MD[14,34]. This suggests that visual experience during the critical period is essential for the development of normal function, rather than structure, of dLGN projections to superficial layers of V1. However, future studies are needed to dissect whether the form, as well as function, of binocular thalamocortical projections are impaired by MD.

In this study, we examined the role of early visual experience in shaping visual response properties of dLGN inputs to binocular visual cortex. Our findings confirm the existence of binocular dLGN responses reported in recent studies[17–19] and further demonstrate that binocular thalamocortical afferents and their interocular matching of visual responses are particularly susceptible to sensory deprivation during the critical period for ocular dominance plasticity. In contrast, overall SF processing in dLGN inputs remains relatively intact following critical-period MD despite V1 neurons displaying a marked acuity loss. Our findings provide further evidence for the hypothesis that distinct developmental mechanisms are involved in fine-tuning of neural circuits underlying binocularity *vs.* acuity[25].

Given that binocular dLGN afferents were found to display particularly strong visual responses, it is tempting to speculate whether these high-fidelity axons may carry visual signals that are critical for binocular vision and disparity selectivity[35]. Our result is in agreement with a previous finding showing that binocular dLGN cells receive inputs from a larger number of retinal ganglion cells compared to monocular dLGN cells[21]. Our surprising finding that the ipsilateral eye is placed at a greater disadvantage when binocular dLGN responses become mismatched hints at an interesting possibility that the ipsilateral input relies on the contralateral input for binocular matching. This is in line with previous findings showing that the ipsilateral pathway develops later and is more vulnerable to developmental manipulations compared to the contralateral pathway[3,4,35–37].

Taken together, our findings demonstrate that binocularity in the early feedforward pathway from dLGN to V1 requires normal visual experience during the critical period to develop properly. While it is likely that interocular competition plays a role, the exact locus of action, cell types and molecular factors involved in this developmental mechanism remain to be elucidated[38]. Given our new findings, it may be necessary to reassess the role for dLGN in visual system development and plasticity, including our own work using inhibitory cell transplantation to reinstate critical-period cortical plasticity[26]. Future work will be needed to disentangle the relative contributions of thalamic and cortical mechanisms of binocular system development. Furthermore, it will be important to determine whether binocularity in the primate dLGN[20] is also vulnerable to loss during the critical period of development, in order to assess the significance of these findings in the context of amblyopia.

AUTHOR CONTRIBUTIONS

C.Y.H. and S.P.G. conceived experiments, C.Y.H., K.A. and K.J.S. performed experiments, C.Y.H., K.A., K.J.S., J.Z. and C.F. analyzed data, C.Y.H., D.G., J.Z. and J.P.P. built custom software, D.X.F.V. generated preliminary data, C.Y.H. and S.P.G. wrote the manuscript.

ACKNOWLEDGMENTS

This work was supported by NIH DP2 grant (NEI EY024504) to S.P.G., and CIHR Postdoctoral Fellowship and Knights Templar Eye Foundation Grants to C.Y.H.

REFERENCES

1. Wiesel, T. & Hubel, D. *J. Neurophysiol.* **26**, 1003–1017 (1963).
2. Blakemore, C., Garey, L.J. & Vital-Durand, F. *J. Physiol.* **283**, 223–262 (1978).
3. Dräger, U.C. *J. Neurophysiol.* **41**, 28–42 (1978).
4. Gordon, J.A. & Stryker, M.P. *J. Neurosci.* **16**, 3274–3286 (1996).
5. Pizzorusso, T. et al. *Proc. Natl. Acad. Sci. U. S. A.* **103**, 8517–8522 (2006).
6. Heimel, J.A., Hartman, R.J., Hermans, J.M. & Levelt, C.N. *Eur. J. Neurosci.* **25**, 795–804 (2007).
7. Levi, D.M. *Vis. Neurosci.* **30**, 277–87 (2013).
8. Wiesel, T.N. & Hubel, D.H. *J. Neurophysiol.* **26**, 978–993 (1963).
9. Blakemore, C. & Vital-Durandt, F. *J. Physiol.* **380**, 493–511 (1986).
10. Levitt, J.B., Schumer, R.A., Sherman, S.M., Spear, P.D. & Movshon, J.A. *J. Neurophysiol.* **85**, 2111–29 (2001).
11. Sherman, S.M., Hoffmann, K.-P. & Stone, J. *J. Neurophysiol* **35**, 532–541. (1971).
12. Duffy, K.R., Holman, K.D. & Mitchell, D.E. *Vis. Neurosci.* **31**, 253–61 (2014).
13. Antonini, A. & Stryker, M.P. *Science* **260**, 1819–21 (1993).
14. Antonini, A., Fagiolini, M. & Stryker, M.P. *J. Neurosci.* **19**, 4388–4406 (1999).
15. Hess, R.F., Thompson, B., Gole, G. & Mullen, K.T. *Eur. J. Neurosci.* **29**, 1064–70 (2009).
16. Allen, B., Spiegel, D.P., Thompson, B., Pestilli, F. & Rokers, B. *Vision Res.* **114**, 48–55 (2015).
17. Howarth, M., Walmsley, L. & Brown, T.M. *Curr. Biol.* **24**, 1241–1247 (2014).
18. Sommeijer, J.-P. et al. *Nat. Neurosci.* **20**, 1715–1721 (2017).
19. Jaepel, J., Hübener, M., Bonhoeffer, T. & Rose, T. *Nat. Neurosci.* **20**, 1708–1714 (2017).
20. Zeater, N., Cheong, S.K., Solomon, S.G., Dreher, B. & Martin, P.R. *Curr. Biol.* **25**, 3190–3195 (2015).
21. Rompani, S.B. et al. *Neuron* **93**, 767–776 (2017).

22. Wekselblatt, J.B., Flister, E.D., Piscopo, D.M. & Niell, C.M. *J. Neurophysiol.* **115**, 2852–2866 (2016).

23. Salinas, K.J., Velez, D.X.F., Zeitoun, J.H., Kim, H. & Gandhi, S.P. *J. Neurosci.* **37**, 10125–10138 (2017).

24. Prusky, G.T. & Douglas, R.M. *Eur. J. Neurosci.* **17**, 167–173 (2003).

25. Stephany, C.-E. et al. *J. Neurosci.* **34**, 11631–11640 (2014).

26. Davis, M.F. et al. *Neuron* **86**, 1055–1066 (2015).

27. Durand, S. et al. *J. Neurosci.* **36**, 12144–12156 (2016).

28. Wang, B.S., Sarnaik, R. & Cang, J. *Neuron* **65**, 246–256 (2010).

29. Gu, Y. & Cang, J. *Elife* **5**, 1–14 (2016).

30. Levine, J.N., Chen, H., Gu, Y. & Cang, J. *J. Neurosci.* **37**, 5822–5833 (2017).

31. Marshel, J.H., Kaye, A.P., Nauhaus, I. & Callaway, E.M. *Neuron* **76**, 713–720 (2012).

32. Cruz-Martín, A. et al. *Nature* **507**, 358–61 (2014).

33. Sun, W., Tan, Z., Mensh, B.D. & Ji, N. *Nat. Neurosci.* **19**, 308–315 (2015).

34. Coleman, J.E. et al. *J. Neurosci.* **30**, 9670–9682 (2010).

35. Scholl, B., Pattadkal, J.J. & Priebe, N.J. *J. Neurosci.* **37**, 6517–6526 (2017).

36. Sretavan, D.W. & Shatz, C.J. *J. Comp. Neurol.* **255**, 386–400 (1987).

37. Godement, P. et al. *Development* **34**, 7976–7987 (2014).

38. Kerschensteiner, D. & Guido, W. *Vis. Neurosci.* **34**, E008 (2017).

FIGURE LEGENDS

Fig. 1. Selective loss of binocular thalamocortical boutons following critical-period MD. **a**, Schematic of dLGN virus injection and GCaMP6s expression in thalamocortical axons in V1 (see Methods). **b**, Experimental timeline. **c**, *In vivo* two-photon Ca^{2+} imaging of visual responses were performed in awake head-fixed mice. **d**, An example cranial window with the binocular zone mapped using widefield intrinsic signal imaging (scale bar 1 mm). **e**, An example field of view (summed projection) of dLGN boutons imaged in L1-2/3 of a control mouse's bV1. Visually responsive boutons (see Methods for criteria) were color-coded according to peak SF during contralateral- (left) and ipsilateral-eye (right) viewing (scale bar 10 µm). **f**, Same dataset as in **e** but color-coded for ocular dominance (see Methods). **g**, Ca^{2+} signals in a binocular (top) and two monocular (middle, bottom) example boutons in response to drifting grating stimulation of contralateral or ipsilateral eye (gray: individual traces, black: mean trace, purple and orange bars: time of stimulus presentation; bouton image scale bar 2 µm). Responses to 8 orientations at peak SF are shown. **h**, Number of visually responsive boutons per field in control *vs.* MD mice (mean ± SEM per field, n = 17 control, 15 MD fields; linear mixed-effects model, effect of MD for ipsi-only: P = 0.62, binocular: P = 0.02, contra-only: P = 0.08). **i**, Ocular dominance index distribution of boutons in control and MD mice (mean ± SEM per field, n = 17 control, 17 MD fields). **j**, Violin and overlaid box plots of mean response amplitudes (R_{pref}) of boutons (linear mixed-effects model, effect of control *vs.* MD: P = 0.50, binocular *vs.* monocular: $P = 2.2 \times 10^{-16}$). In box plots, the central mark indicates the median and the bottom and top edges indicate the 25th and 75th percentiles, respectively. **k**, Percentage of visually responsive V1 L2/3 excitatory neurons per field in control *vs.* MD mice (mean ± SEM per field, n = 10 control, 12 MD fields; linear mixed-effects model, control *vs.* MD for ipsi-only: P = 0.14, binocular: P = 0.01, contra-only: P = 0.66). **l**, Ocular dominance index distribution of V1 neurons in control and MD mice (mean ± SEM per field). **m**, Fraction of visually responsive dLGN boutons (left) and V1 neurons (right) that were ipsi-only, contra-only or binocular (boutons: $\chi^2(2) = 38.3$, $P = 4.8 \times 10^{-9}$, n = 2866 boutons in 5 control mice, 2975 boutons in 6 MD mice; V1 neurons: $\chi^2(2) = 17.4$, $P = 1.6 \times 10^{-3}$, n = 1051 neurons in 9 control mice, 1145 neurons in 4 MD mice). All panels: $^{ns}P > 0.05$, $^{*}P < 0.05$, $^{***}P < 0.001$, $^{****}P < 0.0001$.

Fig. 2. Intact SF processing in thalamocortical boutons following critical-period MD. **a**, Example fields of view of dLGN boutons imaged in bV1, color-coded according to peak SF of bouton during contralateral- *vs.* ipsilateral-eye presentation in control and MD mice (scale bar 10 μm). **b**, Mean probability distribution of peak SF in dLGN boutons, shown separately for binocular-contra, binocular-ipsi, monocular-contra, monocular-ipsi responses (mean ± SEM of by-animal values, n = 5 control *vs.* 6 MD mice). **c**, Mean peak SF of boutons in control *vs.* MD mice (mean ± SEM of by-animal values, 3-way ANOVA, control *vs.* MD: P = 0.56, binocular *vs.* monocular: P = 0.04, contra *vs.* ipsi: P = 0.13). **d**, Mean probability distribution of peak SF in V1 L2/3 excitatory neurons (mean ± SEM of by-animal values, n = 9 control *vs.* 4 MD mice). Note leftward shift of SF distribution curves in MD mice compared to controls. For **b** and **d**, mean values were fitted with a local regression smoothing function. **e**, Mean peak SF of V1 L2/3 neurons in control *vs.* MD mice (mean ± SEM of by-animal values, 3-way ANOVA, control *vs.* MD: P = 0.007, binocular *vs.* monocular: P = 0.01, contra *vs.* ipsi: $P < 10^{-6}$; post-hoc tests: control *vs.* MD in binocular-contra: P = 0.004, binocular-ipsi: P = 0.32, monocular-contra: P = 0.03, monocular-ipsi: P = 0.21). All panels: $^{*}P < 0.05$, $^{**}P < 0.01$.

Fig. 3. Interocular mismatch in thalamocortical boutons following critical-period MD. **a**, Visual response amplitudes of binocular dLGN boutons to preferred SF and orientation (R_{pref}) during contralateral- (y-axis) *vs.* ipsilateral-eye (x-axis) viewing. Black open circles indicate mean values. **b**, Ocular dominance distribution of binocular boutons (mean ± SEM per field, n = 17 fields in 5 control mice, 17 fields in 6 MD mice). **c**, Ocular dominance index values of binocular boutons are shifted towards the contralateral (deprived) eye in MD mice (Wilcoxon rank sum test: P = 0.02). **d**, Example contralateral- *vs.* ipsilateral-eye SF tuning curves of binocular dLGN boutons in control (top) and MD (bottom) mice (2 examples each). **e**, Proportion plots of contralateral- *vs.* ipsilateral-eye peak SF in binocular boutons in control and MD mice. Unity (dotted line) represents perfect match. **f**, Interocular difference in peak SF (contra – ipsi) for binocular boutons is greater in MD mice (Wilcoxon rank sum test: P = 0.0008). **g**, Example contralateral- *vs.* ipsilateral-eye orientation tuning curves of binocular dLGN boutons in control and MD mice (2 examples each). **h**, Scatter plot of preferred grating orientation of binocular dLGN boutons during contralateral- *vs.* ipsilateral-eye viewing. **i**, Interocular difference in preferred orientation for binocular boutons is greater in MD mice

(Wilcoxon rank sum test: $P = 0.0028$). For **d** and **g**, purple traces are from contralateral-eye trials; orange traces are from ipsilateral-eye trials; solid traces are mean response amplitudes; dotted traces are fitted curves based on the mean values. All panels: $n = 171$ *vs.* 81 binocular boutons in 5 control *vs.* 6 MD mice, respectively. $^{*}P < 0.05$, $^{**}P < 0.01$, $^{***}P < 0.001$.

METHODS

Animals

For thalamocortical axon imaging, we used wildtype C57BL/6 mice (Strain No. 027, Charles River) and VGLUT2-Cre mice (Vglut2-ires-cre; Stock No. 016963, Jax Labs). VGLUT2-Cre homozygous mice were bred with wildtype mice to produce heterozygous offspring that were used for imaging. For excitatory V1 neuron imaging, a Camk2a-tTa driver line (Stock No. 007004, Jax Labs) was crossed to a line expressing GCaMP6s under the control of the tetracycline-responsive regulatory element (tetO; Stock No. 024742, Jax Labs) to produce CaMK2a-tTA;tetO-GCaMP6s mice[1]; the founder line was heterozygous for both transgenes and maintained by breeding with wildtype mice. Mice were weaned at P19 and co-housed with one or more littermate of the same sex until viral injections. All mice were housed in conventional mouse housing conditions, and both male and female mice were used. For all surgeries, body temperature was maintained at ~37.5°C by a feedback-controlled heating pad and eyes were covered with ophthalmic ointment to prevent drying. All protocols and procedures followed the guidelines of the Animal Care and Use Committee at the University of California, Irvine.

Monocular deprivation

Mice were monocularly deprived (MD) during the critical period for ocular dominance plasticity (P19 - 33) by eyelid closure[2]. Under isoflurane anesthesia (2% for induction, 1 - 1.5% for maintenance), the non-deprived eye was covered with ophthalmic ointment and the other eye was kept moist with sterile saline. Eye lashes were trimmed and upper and lower eyelids were sutured closed using two mattress sutures (7-0 silk, Ethicon). Eyes were checked every 2-3 days for proper closure. On the 14th day of MD, the previously closed eye was reopened and carefully checked for any ocular damage under a microscope. If an eye opened prematurely or was found to be damaged, the animal was excluded from the study. Eye health was further monitored for 1 - 2 weeks following eye reopening.

GCaMP6s virus delivery

For thalamocortical axon imaging, we initially injected AAV1.Syn.GCaMP6s virus into the dorsolateral geniculate nucleus of the thalamus (dLGN) in wildtype C57BL/6 mice but we found that this approach led to labeling of some V1 cell somata. Thus, we employed another approach of injecting AAV1.Syn.Flex.GCaMP6s virus into dLGN in VGLUT2-Cre mice. Since vesicular glutamate transporter 2 (VGLUT2) is predominantly expressed by thalamic neurons[3], we were able to restrict GCaMP6s expression specifically to dLGN neurons using this approach, with little to no cells being labeled in V1. Results from the two approaches were similar and data from 3 wildtype and 8 VGLUT2-Cre mice used for functional imaging were combined for analysis. Viral vectors were obtained from Penn Vector Core.

For dLGN injections, mice (P58 - 80; mean: P67) were placed in a stereotaxic frame under isoflurane anesthesia (2% for induction, 1 - 1.5% for maintenance). Mice were injected with lactated Ringer's solution and carprofen (5 mg/kg, s.c.) for hydration and analgesia. Scalp was retracted and a small burr hole was made at the injection site using a pneumatic drill. Coordinates used for targeting dLGN was ~2.2 mm posterior, ~2.2 mm lateral from bregma, and ~2.6 mm deep from the brain surface. Viral vectors diluted to the final titre of ~1 x 10^{12} GC/ml were loaded into a glass pipette and injected into dLGN in one hemisphere (total volume: 80 nl, rate: 8 nl/min). In MD mice, the hemisphere contralateral to the deprived eye was injected. The skull and injection site were kept moist with saline during the injection. Following surgery, mice were placed on a heat pad to recover and monitored for post-operative health.

Cranial window implantation

Headplate attachment and craniotomy were performed in one surgery following previously reported procedures[4]. Briefly, mice were anesthetized with isoflurane (2% for induction, 1 - 1.5% for maintenance) and topical lidocaine (2%) was applied to provide analgesia. With the head secured in a stereotaxic frame, the skull was exposed and an approximate location of bV1 was marked. A layer of cyanoacrylic glue (3M Vetbond™) was applied to the skull and a custom-printed black headplate was centered over bV1 and fixed to the skull using black dental acrylic (Ortho-Jet, Lang Dental) at an angle parallel to the imaging site. A craniotomy (4 or 5 mm dia.) was performed and a No. 1 glass coverslip was placed

over the exposed brain and sealed with cyanoacrylic glue and dental acrylic. Mice were placed in a warm cage to recover until mobile and given daily injections of lactated Ringer's and carprofen for at least 3 days and monitored for post-operative health. In MD mice, craniotomy was performed over bV1 contralateral to the deprived eye. Age of mice at craniotomy was P83 - 106 (mean: P94).

Widefield imaging for bV1 mapping

Widefield imaging for bV1 mapping was performed through the cranial window after ≥ 4 days of recovery following craniotomy and age of mice at mapping was P90 - 114 (mean age: P101). For mice used for thalamocortical axon imaging, mapping of binocular V1 was performed using widefield intrinsic signal imaging, following published procedures[4,5]. Briefly, awake mice were placed on a smooth platform, head-fixed and shown contrast-reversing noise stimulus that spanned central 30° of the mouse's visual field. The stimulus was swept either up or down periodically every 20 s. The stimulus was generated by multiplying a band-limited (<0.05 cpd, >2 Hz) binarized spatiotemporal noise movie with a one-dimensional Gaussian spatial mask (30°) using custom Python scripts. Visual stimuli were presented on a gamma-corrected 24" LED monitor (ASUS VG248, 60 Hz refresh rate, 20 cd/m^2 mean luminance) at a viewing distance of 25 cm. Widefield fluorescence images were acquired using a SciMedia THT macroscope (Leica PlanApo 1.0X, 6.5 x 6.5 mm imaging area) equipped with an Andor Zyla sCMOS camera. For visualizing vasculature, a green (530 nm) LED was used. The camera was focused ~600 μm beneath the brain surface, located using vasculature, and intrinsic signals were acquired with a red (617 nm) LED. The stimulus was presented for 5 min under binocular viewing conditions and typically 2 - 3 repeats were run for each condition. Data were analyzed to extract maps of amplitude and phase of cortical responses by Fourier analysis at the frequency of stimulus repetition[6] using custom MATLAB (MathWorks) software. Amplitude was computed by taking the maximum of the Fourier amplitude map smoothed with a 5x5 Gaussian kernel. For Cam2k-tTA;tetO-GCaMP6s transgenic mice, mapping of bV1 was performed using widefield GCaMP6s imaging (blue LED excitation at 465 nm), following similar procedures published previously[4].

In vivo two-photon Ca^{2+} imaging

All imaging was performed in awake head-fixed mice sitting on a smooth tablet surface. Mice were habituated on the imaging setup for 0.5 - 1 hour each day for 1 - 2 days prior to imaging. From the same mouse, imaging was performed typically for 2 - 3 hours per day for 2 - 5 days from different fields of view (age at imaging: P93 - 132, mean: P106). The average time interval between GCaMP6s virus injection and two-photon imaging was 39 days.

A resonant two-photon microscope (Neurolabware) and 920 nm excitation laser (Mai Tai HP, Spectra-Physics) were used for GCaMP6s imaging, following previously published procedures[4] with modifications. A Nikon 16X (NA = 0.8) water-immersion objective was used. For dLGN bouton imaging, fields of view were typically ~220 µm x 260 µm and image sequences were acquired at 8 Hz (990 lines) at depths of 140 ± 37 µm (mean ± SD in 34 fields) below the pia, corresponding to cortical layers 1-2/3. Recordings were confined to anterior and middle parts of bV1. For V1 excitatory neuron recordings, fields were typically ~700 µm x 500 µm, acquired at 7.7 Hz (1024 lines) and recordings were performed in middle bV1 at cortical depths of approximately 200 µm, corresponding to L2/3. Data acquisition was controlled by Scanbox software (Scanbox).

Visual stimuli were generated by custom Python software using PsychoPy 1.8 library. Spherically corrected stimuli were presented on a gamma-corrected 24” LED monitor (Asus VG248, 60 Hz refresh rate, 20 cd/m^2), placed at 25 cm from the mouse’s eyes. The stimuli included full-field drifting sinusoidal gratings (contrast: 99%) of 5 - 6 spatial frequencies (SF; 0.03 - 0.48 or 0.03 - 0.96 cpd, spaced logarithmically) and 8 directions (0 - 315°, in 45° steps) at a temporal frequency of 2 Hz, a blank (uniform luminance) condition, and a full-field flicker (2 Hz) condition. Each trial consisted of a visual stimulus for 2 s and a uniform gray screen for 2 s. Different stimuli were presented in a random order without replacement and typically 8 repeats were run per stimulus condition. Visual stimuli were presented to one eye at a time, either first to the contralateral or ipsilateral eye using an occluder, and the order of eye presentation was chosen randomly for each session. Eyes were monitored using IR-compatible GigE cameras (Allied Vision Mako-131B), typically positioned at 28 cm from the mouse’s eyes and at 45° from the midline. The illumination by the infrared laser (used for two-photon imaging) was used for pupil tracking.

Ca^{2+} imaging data analysis

Custom Python software was used to remove motion artifacts, manually identify dLGN boutons and cells, extract fluorescence traces, and perform batch analyses, according to previously described procedures[4] with modifications. We implemented a motion correction algorithm that corrects for translational artifacts by minimizing the Euclidean distance between frames and a template image, using a Fourier transform approach[7]. The outcome of the motion correction was checked by visualizing the mean intensity of 40 pixels in the middle of the frame throughout the movie. To identify regions of interest (ROIs) as boutons or cell bodies, we used the summed intensity projection of the motion-corrected movies and applied morphological criteria to manually identify them.

All pixel values within the ROI region were averaged to yield the fluorescence trace for the ROI. The fluorescence signal of a cell body at time *t* was determined[8,9] as follows: $F_{cell}(t)=F_{soma}(t)-(R\cdot F_{neuropil}(t))$. R was empirically determined to be 0.7 by comparing blood-vessel intensity of GCaMP6s signal to that in the neuropil. The neuropil signal was estimated by taking the mean of the signal in all pixels within ~3 μm radius outside the cell's outline. Bouton data were treated to a similar neuropil subtraction except that for neuropil, a radius of ~1 μm outside the bouton's outline was used.

To determine a ROI's response to each stimulus trial, the ROI's trace during the stimulation period was first normalized to the baseline fluorescence value averaged over the 0.5 s preceding the stimulus ($\Delta F / F_0$). Then, the mean response amplitude (mean $\Delta F / F_0$) was generated for each stimulus type by averaging the normalized response across all trials of that stimulus. A ROI's spontaneous calcium fluctuation was estimated using the ROI's mean response amplitude during blank stimulus presentation. For each SF, a ROI's responsiveness was determined using a one-way ANOVA ($P < 0.01$) across responses for all orientations for that SF against responses for the blank condition. For most of the analyses in this paper, we restricted our analyses to ROIs whose responses at the peak SF (SF that gave the strongest response) reached statistical significance at $P < 0.01$ (except for data depicted in Fig. 1f ; see below for ODI calculation). In Supplementary Fig. 1, we explored whether lowering or raising the significance level to $P < 0.05$ or $P < 0.005$ affected our results and we found that the effect of MD on binocular bouton number and proportion remained statistically significant under the different criteria. For V1 L2/3 neuron recordings, an additional criterion

was placed such that only cells whose mean $\Delta F / F_0$ for their preferred stimulus (R_{pref}) was ≥ 0.05 were included in further analyses.

For each ROI, the preferred orientation (θ_{pref}) was determined at the ROI's peak SF, by calculating half the mean of the directional vectors weighted by the response F(θ) at each orientation as follows:

$$\Theta_{pref} = \frac{\Sigma_i F(\Theta_i) e^{2i\Theta_i}}{2\Sigma_i F(\Theta_i)}$$

For each SF, an orientation tuning curve was obtained by fitting a sum of Gaussians function on mean response amplitudes for the eight orientations. The response amplitude at the preferred orientation based on the fitted values was designated as $R(\theta_{pref})$. To fit a SF tuning curve, response amplitudes at the preferred orientation (θ_{pref}) across the spatial frequencies were fitted with a Gaussian function. The bandwidth was calculated by taking the square root of the width at half the maximum of the fit. R_{pref} is the mean amplitude of the ROI's response to its preferred grating (preferred orientation and SF).

Orientation and direction selectivity for a ROI was determined using a method based on circular variance of the cell's response as follows:

$$gOSI = \frac{\sqrt{(\Sigma_i F(\Theta_i)\sin 2\Theta_i)^2 + (\Sigma_i F(\Theta_i)\cos 2\Theta_i)^2}}{\Sigma_i F(\Theta_i)}$$

$$gDSI = \frac{\sqrt{(\Sigma_i F(\Theta_i)\sin \Theta_i)^2 + (\Sigma_i F(\Theta_i)\cos \Theta_i)^2}}{\Sigma_i F(\Theta_i)}$$

Ocular dominance index (ODI) for each ROI was calculated as (C – I) / (C + I), where C is R_{pref} for contralateral-eye responses and I is R_{pref} for ipsilateral-eye responses. In cases where no significant response was detected for one of the eyes according to the responsiveness criteria described above, R_{pref} for that eye was set to zero. Thus, responses that were purely driven by the contralateral- *vs.* ipsilateral eye stimulation were given ODI values of 1 and -1, respectively. The method of estimating ODI differed for data depicted in Fig. 1f only; color-coding was based on ODI values calculated according to the same formula as above, except that if one eye did not meet the responsiveness criteria, its R_{pref} was not set to zero. Thus, if one of the eyes' responses passed the responsiveness criteria, the other eye's R_{pref} was used to calculate ODI in Fig. 1f.

Histological procedures and anatomical data analysis

After the last imaging session, mice were anesthetized and transcardially perfused with saline and 4% paraformaldehyde. Age of mice at perfusion was P112 - 142 (mean: P119). Brains were extracted, post fixed and cryoprotected with 30% sucrose. The brain was sectioned coronally in 50 µm using a frozen sliding microtome (Microm HM450, Thermo Scientific). Tissue was processed for GFP immunostaining in free floating sections as follows. Sections were blocked for 1 hour at room temperature with 0.5% Triton-X (T8787, Sigma) and 10% BSA (BP1600-100, Fisher) in PBS, then incubated overnight at room temperature with chicken anti-GFP antibody at 1:500 dilution (GFP-1020, Aves Labs). Sections were then washed in PBS and incubated for 2 hours at room temperature with goat anti-chicken IgG antibody tagged with Alexa-488 at 1:1000 dilution (A-11039, Life Technolgies). Sections were further processed for nuclear staining (Hoechst 33342), washed in PBS, coverslipped with Flouromount-G (Southern Biotech) and imaged.

For dLGN sections, we used an epifluorescence microscope (Zeiss Axio Imager 2) with a 10X objective. For cell counting, labeled cells in dLGN sections every 200 µm (3 sections per animal) were manually counted using the cell counter plugin in Fiji. Total number of labeled dLGN neurons as well as the spatial distribution of labeled neurons in dLGN was quantified for each animal (Supplementary Fig. 2 and 6). Functionally imaged brains where post-hoc anatomical data revealed that cells were labeled in the neighboring thalamic nucleus LP were excluded from analysis.

For V1 sections, we first took images using the epifluorescence microscope with a 10X objective. Cortical layers were identified using nuclear staining. In order to estimate thalamocortical axon density, we obtained the mean fluorescence intensity across the cortical depths in a densely labeled area of a fixed size in V1 (186 µm horizontal x 932 µm vertical) of each section and quantified labeling intensity in each layer (Supplementary Fig. 7). To get a more accurate estimate of the axon density, we sought to segment axons from the images. For this, z-stack images were taken of V1 sections every 200 µm (3 sections per animal) using a 20X objective (NA = 1.0) on a Zeiss LSM700 confocal microscope. Images were rotated and cropped to include only superficial layers (L1 and L2/3) in a densely labeled volume of a fixed size in V1 (100 µm horizontal x 242 µm vertical x all z slices), which corresponds to the layers that were functionally imaged using *in vivo* two-photon Ca^{2+}

imaging. Open source neuron tracing software neuTube[10] with custom modifications was used to detect axons automatically. The output traces were filtered to remove abnormally large radius nodes, branching points and isolated nodes. From visual inspection, the auto-segmentation did not detect all visible axons, so the tracing was supplemented by manual tracing by a blinded experimenter. From this final set of traces, we quantified the total axon length per volume and axon radius of thalamocortical axons in V1 L1-2/3 (3 sections per animal).

Statistical analysis

The statistical determination of visual responsiveness is described in detail above; the ANOVA tests for responsiveness, curve-fitting for orientation and SF tuning and related selectivity/bandwidth calculations were performed in custom Python routines. Plotting of fluorescence traces, example tuning curves and overlay of vector graphics on images were done using MATLAB or Python scripts. All other statistical analyses and data plotting were performed using custom software in R[11]. In addition to conventional statistics (Chi-squared tests, T-tests, Wilcoxon rank sum tests, 2- and 3-way ANOVAs, Kolmogorov-Smirnov tests), multilevel statistics were employed in some cases to take into account the nested design of our data (*e.g.*, boutons, neurons, sections nested inside mice). Multilevel linear mixed-effects models with Satterthwaite's approximation were used, with experimental variables (*e.g.*, control *vs.* MD) as fixed variables and mouse ID as a random variable. For each analysis, the exact statistical test used and sample sizes are described in figure legends. All tests were two-tailed. Data are reported as mean ± SEM unless otherwise noted.

METHODS REFERENCES

1. Wekselblatt, J.B., Flister, E.D., Piscopo, D.M. & Niell, C.M. *J. Neurophysiol.* **115**, 2852–2866 (2016).
2. Prusky, G.T. & Douglas, R.M. *Eur. J. Neurosci.* **17**, 167–173 (2003).
3. Herzog, E. et al. *J. Neurosci.* **21**, 1-6 (2001).
4. Salinas, K.J., Velez, D.X.F., Zeitoun, J.H., Kim, H. & Gandhi, S.P. *J. Neurosci.* **37**, 10125–10138 (2017).
5. Davis, M.F. et al. *Neuron* **86**, 1055–1066 (2015).
6. Kalatsky, V.A. & Stryker, M.P. *Neuron* **38**, 529-545 (2003).
7. Dubbs, A., Guevara, J. & Yuste, R. *Front. Neuroinform.* **160**, 269-290 (2016).
8. Kerlin, A.M., Andermann, M.L., Berezovskii, V.K. & Reid, R.C. *Neuron* **67**, 858-871 (2010).
9. Chen, T.W. et al. *Nature* **499**, 295-300 (2013).
10. Feng, L., Zhao, T. & Kim, J. *eNeuro* **2**, 1-10 (2015).
11. R Core Team. R Foundation for Statistical Computing (2017).

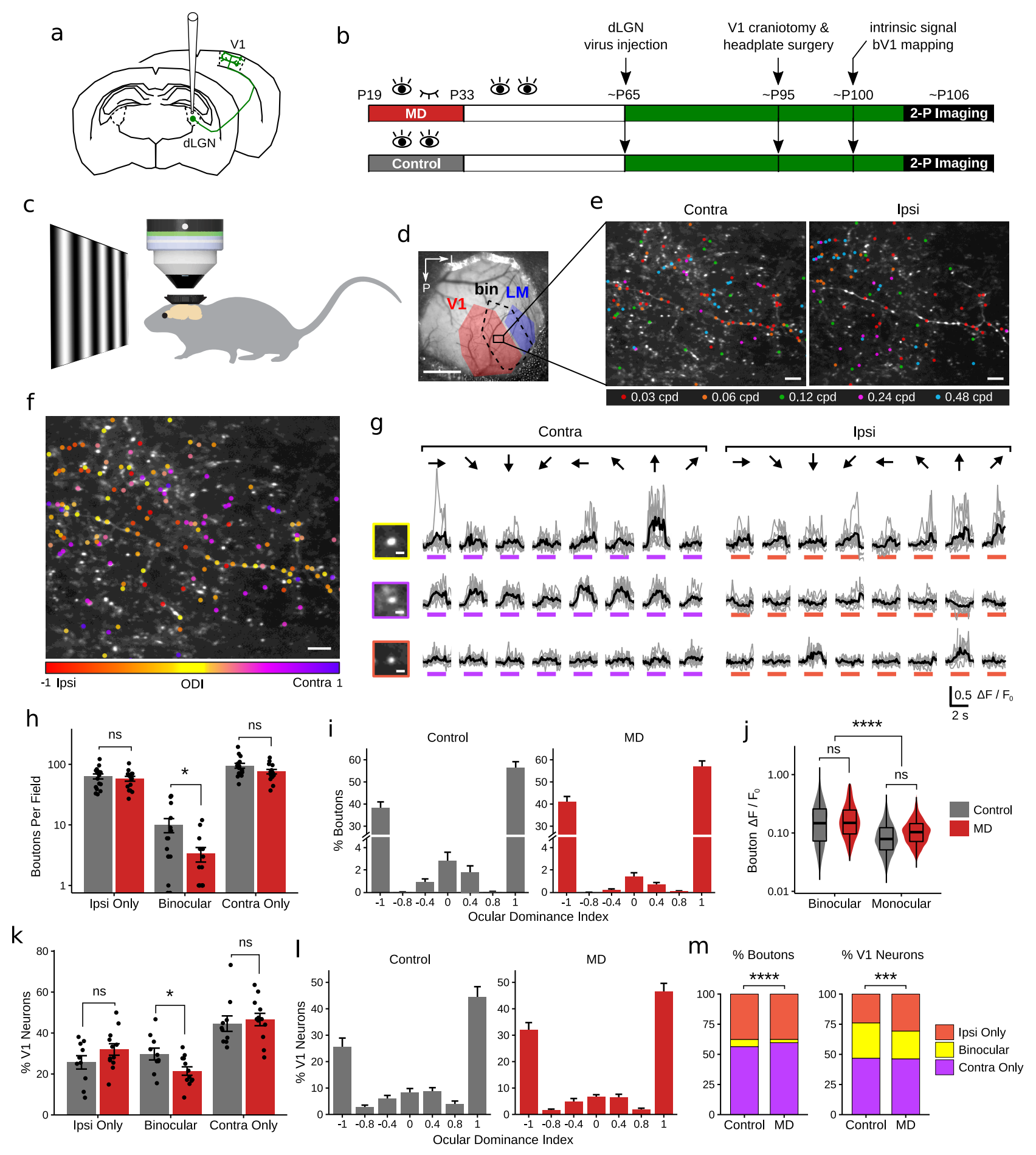
a
V1
dLGN
b
dLGN
virus injection
V1 craniotomy &
headplate surgery
intrinsic signal
bV1 mapping
P19
P33
~P65
~P95
~P100
~P106
MD
2-P Imaging
Control
2-P Imaging
c
d
P
L
bin
LM
V1
e
Contra
Ipsi
0.03 cpd
0.06 cpd
0.12 cpd
0.24 cpd
0.48 cpd
f
-1 Ipsi
ODI
Contra 1
g
Contra
Ipsi
0.5 ΔF / F0
2 s
h
Boutons Per Field
ns
*
ns
Ipsi Only
Binocular
Contra Only
i
Control
MD
% Boutons
Ocular Dominance Index
j
****
ns
ns
Bouton ΔF / F0
Binocular
Monocular
Control
MD
k
% V1 Neurons
ns
*
ns
Ipsi Only
Binocular
Contra Only
l
Control
MD
% V1 Neurons
Ocular Dominance Index
m
% Boutons
****
% V1 Neurons
***
Ipsi Only
Binocular
Contra Only
Control
MD
Control
MD

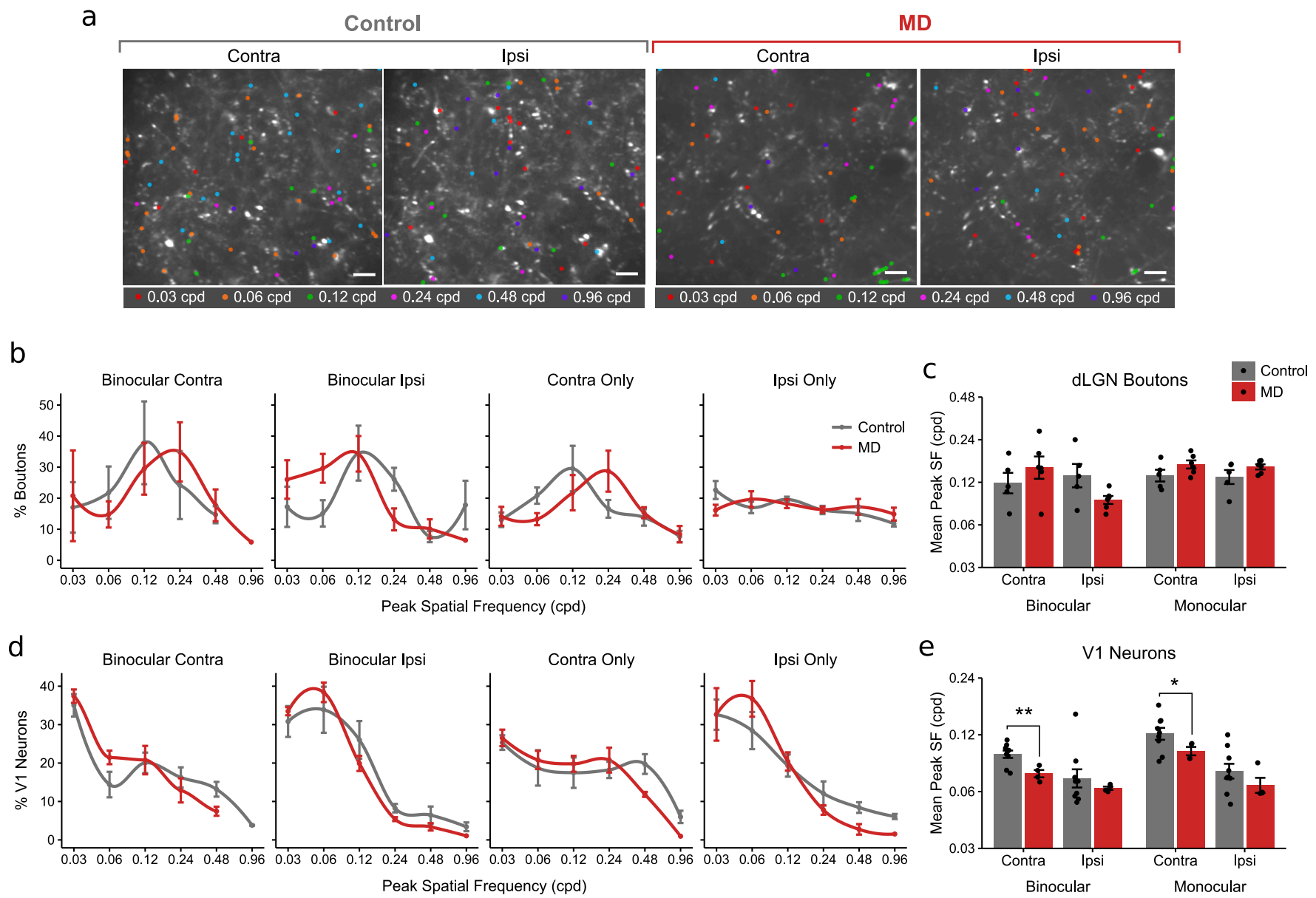
a
Control
MD
Contra
Ipsi
Contra
Ipsi
0.03 cpd
0.06 cpd
0.12 cpd
0.24 cpd
0.48 cpd
0.96 cpd
b
Binocular Contra
Binocular Ipsi
Contra Only
Ipsi Only
% Boutons
Control
MD
Peak Spatial Frequency (cpd)
c
dLGN Boutons
Mean Peak SF (cpd)
Contra
Ipsi
Binocular
Monocular
d
% V1 Neurons
e
V1 Neurons
**
*

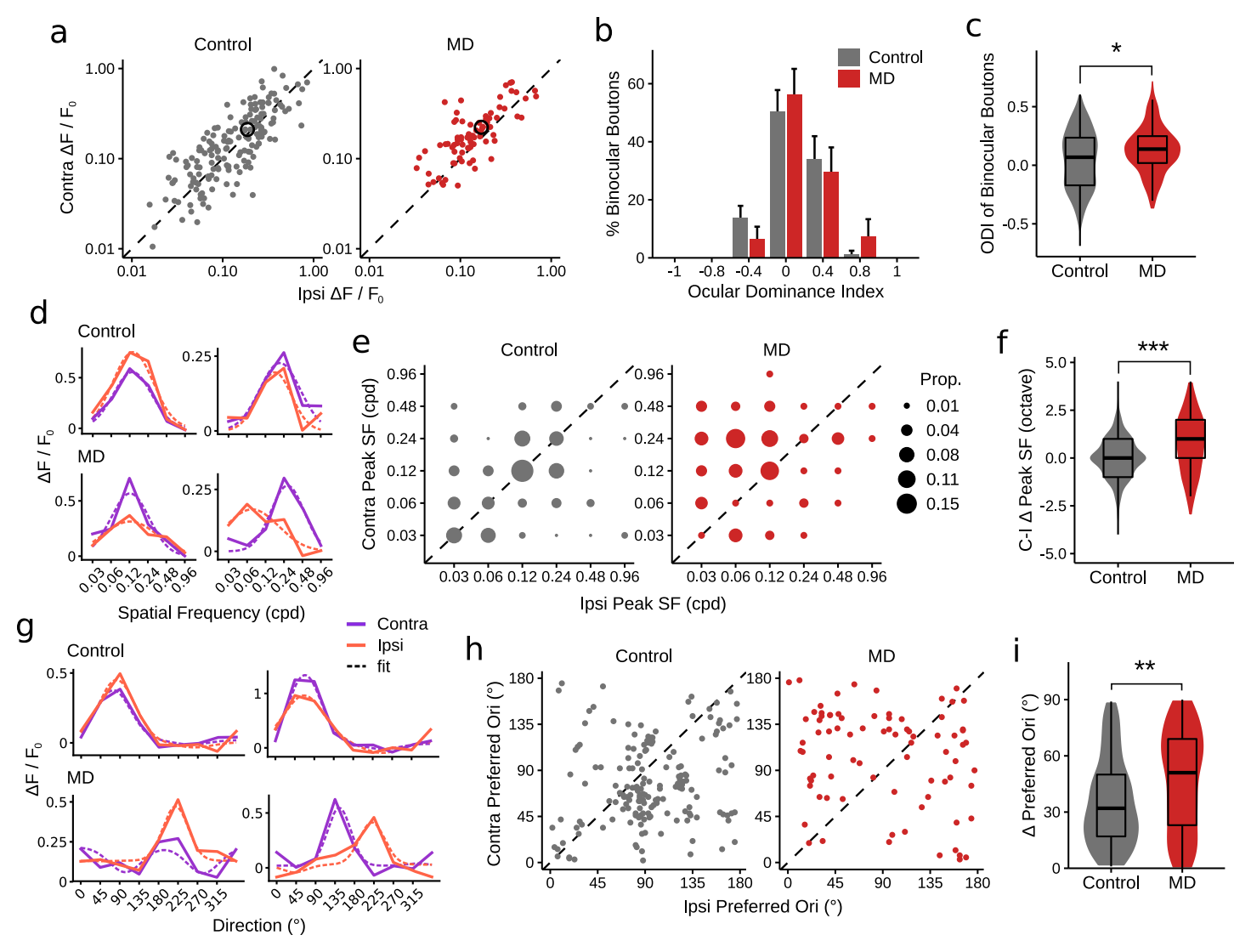
a
Control
MD
Contra ΔF / F0
Ipsi ΔF / F0
1.00
0.10
0.01
b
Control
MD
% Binocular Boutons
Ocular Dominance Index
c
*
ODI of Binocular Boutons
Control
MD
d
Control
MD
ΔF / F0
Spatial Frequency (cpd)
e
Control
MD
Contra Peak SF (cpd)
Ipsi Peak SF (cpd)
Prop.
f
***
C-I Δ Peak SF (octave)
Control
MD
g
Contra
Ipsi
fit
Control
MD
ΔF / F0
Direction (°)
h
Control
MD
Contra Preferred Ori (°)
Ipsi Preferred Ori (°)
i
**
Δ Preferred Ori (°)
Control
MD